Three-dimensional simulations of nanopowder compaction processes by granular dynamics method

G. Sh. Boltachev,* K. E. Lukyashin, V. A. Shitov, and N. B. Volkov
Institute of Electrophysics, Ural Branch of Russian Academy of Sciences, Amundsen Street 106, 620016 Ekaterinburg, Russia
(Received 8 April 2013; published 29 July 2013)

In order to describe and to study the processes of cold compaction within the discrete element method a three-dimensional model of nanosized powder is developed. The elastic forces of repulsion, the tangential forces of "friction" (Cattaneo-Mindlin), and the dispersion forces of attraction (van der Waals–Hamaker), as well as the formation and destruction of hard bonds between the individual particles are taken into account. The monosized powders with the size of particles in the range 10–40 nm are simulated. The simulation results are compared to the experimental data of the alumina nanopowders compaction. It is shown that the model allows us to reproduce experimental data reliably and, in particular, describes the size effect in the compaction processes. A number of different external loading conditions is used in order to perform the theoretical and experimental researches. The uniaxial compaction (the closed-die compaction), the biaxial (radial) compaction, and the isotropic compaction (the cold isostatic pressing) are studied. The real and computed results are in a good agreement with each other. They reveal a weak sensitivity of the oxide nanopowders to the loading condition (compaction geometry). The application of the continuum theory of the plastically hardening porous body, which is usually used for the description of powders, is discussed.

DOI: 10.1103/PhysRevE.88.012209 PACS number(s): 45.70.Cc, 83.10.Rs, 81.07.Wx

I. INTRODUCTION

The compaction of the granulated materials, especially the nanosized powders, is of great importance for the development of the materials with the advanced properties [1–4]. The compression of the nanopowders is a necessary stage in the production of nanostructured materials by the powder metallurgy methods [3–8]. The phenomenology of the continuous media is used for the description of the powder bodies mechanical properties. As an example, the theory of the plastically hardening porous body [5–10] appeared to be a convenient and powerful tool for the theoretical analysis. This theory has a strict justification regarding the sintering or hot compaction of the powders [11,12]. Moreover this theory has been verified experimentally for the processes of the cold compaction of the powders consisting of micron- (or larger) size particles [5,12,13]. In case of the nanosized powders, especially the oxide ones, where the particles cannot deform plastically [14,15], the theory application is very controversial. First of all, such conceptions as the yield stress or the hardening take on a relative nature for the nanopowders. Second of all, the peculiarities of the nanopowder mechanical behavior (like size effect) appear to be outside the continuum theory.

It is well known from the experiments that it is harder to compact the nanopowders compared, for example, to the micron ones [14,16–19]. The size effect in the nanopowder compaction is still poorly studied both experimentally and theoretically. It is believed that low compressibility of the nanopowders is related to a high adhesion between individual particles, which leads to a formation of strong aggregates [20]. The absence of plastic deformation in nanoparticles [14], the covalent bonding between the molecules of adjacent particles [17], van der Waals attractive forces [16,17], and the electrostatic interactions [16] are stated to be the possible reasons for the size effect. The investigations on the gravitational packing of the powders [21,22] show that, in the case of free filling, the density of dry powders decreases under the action of dispersion (van der Waals) forces, which dominate over the gravitational forces when the particles get finer. During cold compaction the particles are exposed to the forces that exceed greatly both gravitational and van der Waals ones. Nevertheless, it has been found recently [20,23–26] that van der Waals forces remain significant and are among the factors that are responsible for the size effect in the nanopowder's compaction.

In this work, we present the simulation results for the compaction of a nanopowder material by the discrete element method [20,21,23,27–37], also known as the granular dynamics method [38–40]. Due to a great extent of sphericity and the nondeformability (strength) of individual particles of oxide nanopowders being studied, the granular dynamics method is particularly attractive and a very promising tool of the theoretical analysis. The nondeformability of the particles with sizes of 10–100 nm is caused by the absence of the defects: the dislocations are pushed out of the particle by the high tension of the "images" [15]. The experiments verify that such particles are deformed elastically and recover their shape after the removal of the load [14]. The present paper is sequential to the investigations [23–26], devoted to two-dimensional (2D) simulations. Here, as distinct from Refs. [23–26], the numerical experiments are performed in a 3D geometry: the particles are spherical with equal diameter; there are both translational and rotational degrees of freedom. The interactions of the particles, in addition to commonly used contact interactions such as Hertz law [41] and Cattaneo-Mindlin law [42–44], involve the dispersion forces of attraction and the possibility of the formation or destruction of solid bridges between particles. The bridges can be formed by the sintering at high temperatures [20] or by a strong particles pressing during the compaction process [45,46]. The presence

*Corresponding author: grey@iep.uran.ru

of dispersion forces allows introducing the particle size into the governing equations [21] and thereby it is the source of the size effect in the theoretical model.

II. INTERPARTICLE INTERACTIONS

A. Normal contact interactions

When the elastic spherical particles with the diameter d are compressed up to a displacement h ($h = d - r$, where r is the center distance of the particles), a contact area with the radius a and the elastic repulsive force f_e appears between them. In the limit of the infinitesimal deformations, when $h/d \ll 1$, the elastic repulsion obeys the Hertz law [41]. However, in the cold compaction processes the nanopowders are subjected to strong external action; a typical pressure amounts to several gigapascals. At that conditions the powder particles receive relatively large deformations, where the ratio h/d can reach 5–10% [25,26]. In the region of such large deformations the Hertz law underestimates sufficiently the elastic force [47–49]. We use the modified Hertz law (so-called "rod model"), given elsewhere [26,50,51], to describe the elastic forces more precisely. According to this rod model

$$\frac{f_e}{Ed^2} = \frac{(h/d)^{3/2}}{3\left(1-\sigma_p^2\right)} - \frac{\pi}{4}\frac{1-\sigma_p}{(1-2\sigma_p)(1+\sigma_p)} \times \left[\frac{h}{d} + \ln\left(1-\frac{h}{d}\right)\right], \quad a = \frac{\sqrt{hd}}{2}, \tag{1}$$

where E is the Young modulus of the particles, σ_p is Poisson's ratio. Equation (1) gives the elastic interaction between the particles up to that moment when a solid bridge appears.

Sticking of the contacts during the high-temperature processing of the powder is implied as a reason of solid bridges formation in Ref. [20]. We suppose that the solid bridges can be formed also due to the strong mechanical connection of the particles that occurs during the compaction process. This results in the overlapping of the surface atoms electron shells and in the formation of the covalent bonds between the molecules of the particles being pressed. In order to take into account this effect, we have introduced the parameter Δr_{ch}, which defines the necessary displacement of the particles. It is supposed that when the interparticle distance r is decreased down to the value of $r_{\min} < d - \Delta r_{ch}$ the solid (chemical) bond between the particles is generated. After the formation of the solid bridge the elastic interaction upon compression (upon the decrease of r) obeys the law (1), but during the tension (upon the increase of r) we have

$$f_e(r, r_{\min}) = f_e(r_{\min}) + \left(\frac{df_e}{dr}\right)_{r_{\min}} (r - r_{\min}),$$
$$\frac{1}{Ed}\left(\frac{df_e}{dr}\right)_{r_{\min}} = -\frac{\sqrt{1-r_{\min}}}{2\left(1-\sigma_p^2\right)} + \frac{\pi/4}{1-2\sigma_p}\left(1-\frac{d}{r_{\min}}\right). \tag{2}$$

The dependence (2) describes the linear correlation between the force f_e and the distance r up to the value $r = r_{\min} + \Delta r_{ch}$. The further increase of r produces the partial breaking of the solid bridge. In order to describe the partial bridge destruction the parameter $r_{\min}$ is increased so that a difference $r - r_{\min}$ remains equal to the value of Δr_{ch}. The total destruction of the bridge occurs when the interparticle distance equals the particle diameter, i.e., $r = d$.

B. Dispersion forces of attraction

The dispersion intermolecular interactions result in the interparticle forces of attraction [52], which is of great importance when simulating nanosized powders. However, the original Hamaker's result [52] is inapplicable within the granular dynamics method due to the singularity of the attractive energy of touching particles. That is why we use the modified Hamaker's formula [23,24,53] to calculate the dispersion force of attraction:

$$f_a(r) = \frac{\pi^2}{3}\frac{\left(nd_0^3\right)^2 \varepsilon d^6}{(r+\alpha d_0)^3[(r+\alpha d_0)^2 - d^2]^2}, \tag{3}$$

where d_0 and ε are the size and energy parameters of the intermolecular interactions, the parameter $\alpha = 0.24$. The latter parameter was determined in Refs. [23,24,53] as the fulfillment of the transition to the interaction of molecules at $d \to d_0$. The parameter $\alpha < 1$ corresponds to the fact that the equilibrium distance between the surfaces of the macroscopic particles (αd_0) must be shorter then the equilibrium distance between two atoms (d_0). This fact is confirmed by the direct molecular dynamics simulations [54].

Equation (3) describes the particles' attraction as long as the distance between the particles $r \geqslant d$. When the particles touch each other ($r = d$) and are pressed further ($r < d$) the attraction force f_a is supposed to be a constant and is equal to its maximal value $f_{a,\max} = f_a(d)$. Figure 1 shows the total force $f_n = f_e - f_a$ of the normal interactions of the particles. Here and below the α phase of aluminium oxide is intended as particle material, and the simulation parameters are $E = 382$ GPa, $\sigma_p = 0.25$, $nd_0^3 = \sqrt{2}$, $d_0 = 0.392$ nm [24]. In contrast to Ref. [24] the parameter ε is assigned the value of $1224k_B$. At that the dispersion force $f_{a,\max}$ corresponds to the adhesive force ($\pi\gamma d$) of the Derjaguin-Muller-Toporov

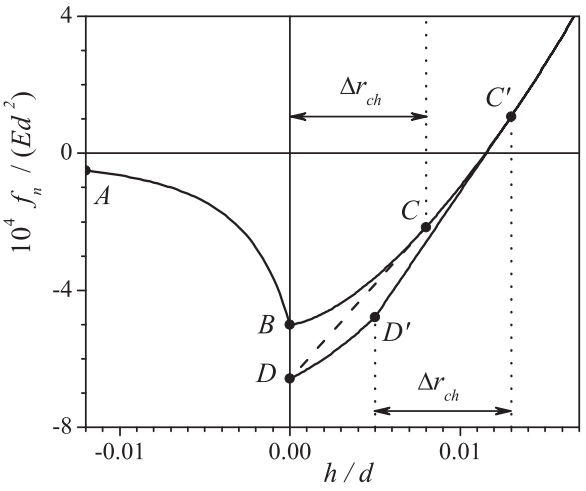

FIG. 1. The total normal force of two particles interaction as a function of the separation $h = d - r$. Calculation parameters are the parameter $\alpha = 0.24$, the particles' diameter $d = 16$ nm, the distance of formation or destruction of the solid bridge $\Delta r_{ch} = 0.008d$.

(DMT) model [55] with the surface energy $\gamma = 1\ \mathrm{J/m^2}$, which represents typical covalent and ionic ceramic materials [20].

When a direct contact is absent the dispersion attraction between the particles, Eq. (3), is described by the AB curve in Fig. 1. At point B (the point of the particle's contact) the attraction force reaches its maximal value $f_{a,\max}$ and the elastic force of repulsion $f_e = 0$. In this way, the maximal attraction of the particles is realized. The further continuous loading corresponds to BCC' curve. Here the particles' attraction force is a constant, but the elastic force increases according to the law of Eq. (1). The interparticle distance, where the elastic force compensates exactly the dispersion force of attraction, i.e., $f_n = f_e - f_a = 0$, is the equilibrium distance r_{eq}. When $r < r_{eq}$ the elastic repulsion force dominates over the attraction force ($f_n > 0$). The contact unloading from the values $h < \Delta r_{ch}$, i.e., before the formation of the solid bridge at the C point, occurs as a reversible process, along the ABC curve again. The unloading from the value $h = \Delta r_{ch}$, i.e., from the C point, where the formation of the solid bridge has occurred, is described by the CD line. This rectilinear segment describes the elastic interaction of the particles as long as the parameter h stays within it. When the D point is reached the destruction of the solid bridge takes place. Here the interaction force switches to the B point and is described by the ABC curve again. When loading up to a C' point (which is to the right of the C point), the rectilinear segment shifts to the $C'D'$ position. If the contact state is shifted to the left of the D' point then C' and D' points are shifted to the left simultaneously, so that the rectilinear segment of $C'D'$ is moved to the CD line. The C' point moving corresponds to the partial breaking of the bridge, i.e., the decreasing of the contact area, which has started at the D' point. It can be noted that parameters, which determine the formation and the destruction of the solid bridge, do not have to be equal, in general. We use the single parameter Δr_{ch} to describe these processes for the purpose of the model simplification only.

Figure 2 demonstrates the mean normal stress on the contact area, which activates the partial (at $h > 0$) or total (at $h = 0$) destruction of the solid bridge,

$$\sigma_u = \frac{1}{\pi a_{ch}^2}\left[f_n(r)|_{r_{\min}=r-\Delta r_{ch}} - f_n(r)|_{r_{\min}=r}\right],$$

$$a_{ch} = \frac{1}{2}\sqrt{d(d - r + \Delta r_{ch})}.$$

One can see that for the values $\Delta r_{ch} \leqslant 0.01$ the maximal values of breaking load σ_u do not exceed the theoretical strength of the particles material, $E/30 \simeq 13$ GPa. The proximity of the parameter σ_u to the theoretical strength is justified by the nanometer size of the particles [20,56–58].

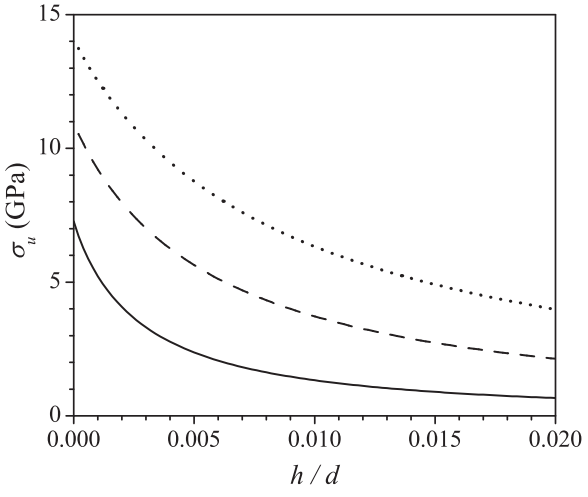

FIG. 2. The mean contact normal stress, which activates the partial bridge destruction (at $h > 0$) or the total fracture of the solid bridge (at $h = 0$). The solid line is for $\Delta r_{ch} = 0.005$, the dashed line is for 0.01, and the dotted line is for 0.015.

C. Tangential shearing force

The tangential displacement of the particles with regard to the contact plane results in the contact area tangential shift, which is characterized by the $\vec{\delta}$ vector, and the emergence of the tangential force $f_t(\delta)$ (where $\delta = |\vec{\delta}|$), which is given by Cattaneo-Mindlin law [42–44]. We use the linearized form of Cattaneo-Mindlin law, which is prevalent by now [29,30],

$$\mathbf{f}_t(\delta) = \frac{\vec{\delta}}{\delta}\ \min\left\{\frac{4Ea\delta}{(2-\sigma_p)(1+\sigma_p)};\ \mu f_e(r);\ \pi a^2\sigma_b\right\}, \quad (4)$$

where μ is the friction constant, σ_b is the critical transverse stress (or the fracture stress), which determines the shearing strength of the material. The authors of Ref. [20] supposed σ_b to be 2 GPa. However, the fracture stress of nanosized bodies can be appreciably larger, right up to the values of $\sigma_b \simeq 0.03E$ [57,58].

When the solid bridge between the particles being in contact is formed, the limitation, connected with Coulomb friction, is withdrawn and law (4) looks like

$$\mathbf{f}_t(\delta) = \frac{\vec{\delta}}{\delta}\ \min\left\{\frac{4Ea_{ch}\delta}{(2-\sigma_p)(1+\sigma_p)};\ \pi a_{ch}^2\sigma_b\right\}. \quad (5)$$

If at the moment, when the breaking point ($f_{M,\max} = \pi a_{ch}^2\sigma_b$) is reached, the interparticle distance $r < (d - \Delta r_{ch})$ then the partial destruction of the solid bridge occurs and the parameter $r_{\min}$ is assigned to the current value of r. Otherwise, if the interparticle distance $r > (d - \Delta r_{ch})$ then the total destruction occurs, but the contact between the particles remains and is described by Eq. (4).

D. Surface pivoting moment

The tangential interaction of the particles being in contact, when pivoting upon the contact axis, is given by Reissner-Sagoci law [59],

$$M_p(\theta_p) = \frac{8Ea^3}{3(1+\sigma_p)}\,\theta_p, \quad (6)$$

where M_p is the surface moment, θ_p is the turn angle of the contact area, i.e., the half angle of the turn of one particle regarding the other. The rigorous solution of the pivoting problem was given by Jäger [60]. Reissner-Sagoci law corresponds to the linearized Jäger law, i.e., the limit of $\theta_p \to 0$. In the region of large values of θ_p the maximal value of the surface moment M_p is confined by Coulomb's friction

law:

$$M_{p,\max}(a)=\mu_f M(a),\quad M(a)=-2\pi\int_0^a \sigma_{zz}(\rho)\rho^2 d\rho, \qquad (7)$$

where $\sigma_{zz}(\rho)$ is the radial distribution of normal stress in the contact area. In the case of the rod model (1) being used we have [50,51]

$$\sigma_{zz}(\rho) = -\frac{4E}{\pi d\left(1-\sigma_p^2\right)}(a^2-\rho^2)^{1/2} - \frac{E(1-\sigma_p)}{(1-2\sigma_p)(1+\sigma_p)}\ln\left(\frac{d^2-4\rho^2}{d^2-4a^2}\right). \qquad (8)$$

It gives

$$M(a) = \frac{\pi E a^4}{2d\left(1-\sigma_p^2\right)} + \frac{\pi E d^3(1-\sigma_p)}{3(1+\sigma_p)(1-2\sigma_p)} \times\left[\frac{1}{4}\ln\left(\frac{d+2a}{d-2a}\right)-\frac{a}{d}-\frac{4}{3}\frac{a^3}{d^3}\right]. \qquad (9)$$

As a result, the tangential interaction is described by the expression

$$M_p(\theta_p)=\min\left\{\frac{8Ea^3}{3(1+\sigma_p)}\,\theta_p;\ \mu_f M(a);\ \frac{\pi}{2}a^3\sigma_b\right\}. \qquad (10)$$

The limitation of M_p, which is caused by the shearing strength σ_b of the material, corresponds to the similar limitation in Ref. [20].

When the solid bridge is formed, like in case of shearing load f_t, the expression (10) for the surface moment $M_p(\theta_p)$ is replaced by the following one:

$$M_p(\theta_p)=\min\left\{\frac{8Ea_{ch}^3}{3(1+\sigma_p)}\,\theta_p;\ \frac{\pi}{2}a_{ch}^3\sigma_b\right\}. \qquad (11)$$

If at the moment, when the breaking point ($M_p=\pi a_{ch}^3\sigma_b/2$) is reached, the interparticle distance $r<(d-\Delta r_{ch})$ then the partial destruction of the solid bridge occurs and the parameter $r_{\min}$ is assigned to the current value of r. Otherwise, if the interparticle distance $r>(d-\Delta r_{ch})$ then the total destruction occurs, but the contact between the particles remains and is described by the law of Eq. (10).

E. Contact elasticity of flexure

It is known that microparticles (or larger particles) are possessed of some friction regarding the rolling, which is characterized by the rolling friction coefficient μ_r (for example, see Refs. [29,33,35]). The sources of rolling resistance are the processes of the plastic deformation in the contact region. Since we simulate the nanosized powders, which particles are not liable to the plastic deformation, we neglect the rolling friction in the absence of a strong bond between the particles. However, when the solid bridge is formed between the particles, the contact becomes elastic to the rolling of the particles (or elasticity of flexure). It is described by [see [61], p. 272, Eq. (4.5)]

$$M_r(\theta_r)=\min\left\{\frac{4}{3}\frac{Ea_{ch}^3}{1-\sigma_p^2}\,\theta_r;\ \frac{1}{3}\,a_{ch}f_e\right\}, \qquad (12)$$

where M_r is the rolling moment, and θ_r is the turn angle of the contact area in the direction, which is orthogonal to the contact axis. The first term in braces is the Lurie law for the interaction between an inclined stamp and half space. The maximal moment value, $a_{ch}f_e/3$, corresponds to the emergence of a tensile load at the stamp periphery. In contrast to cases of shearing or pivoting loads, the decrease of the contact area does not occur when the maximal rolling moment is reached. It is supposed that the rolling is realized here and the contact area with the fixed size moves over the surface of the particles.

III. GENERATING THE INITIAL STRUCTURES

In the first stage a model cell with the sizes (x_{cell}; y_{cell}; z_{cell}) is filled by the initial structure with a given number (N_p) of the particles. This structure corresponds to the initial filling of the powder in a natural experiment. So, based on the physical considerations, the structure has to be connected, i.e., it should not contain "suspended" (i.e., not in contact with the environment) particles or clusters. In addition, assuming that the initial powder filling in the natural experiment is sufficiently homogeneous and isotropic, the initial structure in computer simulations should have similar properties. At last, as the computational capability is not possible to simulate the compaction of macroscopic amounts of the powder, we simulate the so-called representative element and set the periodic boundary conditions on the faces of the model cell. Therefore, to avoid the undesirable edge effects the structure being generated should be periodic (from the outset) in the translation direction of the model cell. In order to meet these requirements we have developed the following algorithm.

The coordinates of the first particle in the cell are assigned randomly. From the last particle, placed in the cell (with the coordinates $\mathbf{r}_0$), a ray is set in a direction of random unit vector $\mathbf{l}_0$. An attempt is made to place a new particle on this ray. For this purpose, we analyze the overlap of the imaginary cylinder with the radius r_{eq}, which is centered on the given ray, with the other particles. Let the jth particle of the filling have the coordinates $\mathbf{r}_j$. Then the distance along the ray up to the point of the closest convergence with the jth particle is $l_d=(\mathbf{r}_j-\mathbf{r}_0)\mathbf{l}_0$, and the shortest distance from the jth particle to the ray is $l_p=[(\mathbf{r}_j-\mathbf{r}_0)^2-l_d^2]^{1/2}$. The point on the ray located at the distance $l_d+(r_{eq}^2-l_p^2)^{1/2}$ from $\mathbf{r}_0$ is assumed to be a possible place for the new particle. The following conditions allow us to consider the jth particle as the potential candidate for the new particle placing: (1) $l_d\geqslant 0$; (2) $l_p\leqslant r_{eq}$; (3) the new particle does not overlap other particles. The equality of $l_d=0$ takes place when the particle with the coordinates $\mathbf{r}_0$ (the origin of the ray) acts as the jth particle. From a number of possible candidates, we choose one that has the minimum number of neighbors in a sphere of the given radius (r_{meso}). In the case of the equal number of neighbors we choose the candidate which is farthest from the origin of the ray. It should be noted that we analyze all the images of the particles located in the nearest images of the model cell along the ray. When a location for the new particle has been chosen at the equilibrium distance r_{eq} from some jth particle, the closest position is determined, where the new particle is in contact with two particles, i.e., with the jth particle and with another, already placed, one. This is the position where the final placement of the new particle takes place.

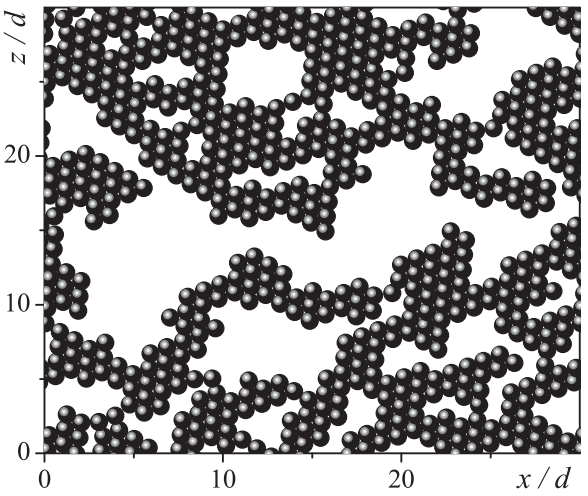

FIG. 3. An example of an initial structure in 2D geometry. The cell sizes are $x_{\text{cell}} = z_{\text{cell}} = 30d$, the number of the particles is $N_p = 600$.

Figure 3 represents an example of the powder structure, which is generated by the algorithm described above in the case of 2D geometry (in 3D geometry the structure images are not so clear). It can be seen that this algorithm makes it possible to create an isotropic distribution of the particles which form a connected cluster. In 3D geometry the cluster consists almost exclusively of the chains with the thickness of two particles. The joint positions of the neighboring chains can be considered as exceptions. So, the average coordination number k of the initial structures is exactly 4 in the absence of the dispersion forces, i.e., when $r_{eq} = 1$. The presence of the dispersion forces reduces the value of the equilibrium distance r_{eq} and, as a result, increases slightly the average coordination number. For example, at $d = 9.7$ nm and $\varepsilon = 1224k_B$ the numerical experiments give $k = 4.0062 \pm 0.0007$. Figure 3 shows that in 2D geometry the situation is different. When placing a new particle in contact with two existing particles, even in the absence of the dispersion forces ($r_{eq} = 1$), there is a high probability of the contact with other particles due to the formation of the regular hexagonal packing of the disks on the plane. The latter, of course, leads to a significant increase of the average coordination number of the initial structure in 2D geometry.

The minimum number (N_1) of the particles in a model cell is determined by the requirement of emergence of the infinite connected cluster, which is formed by cross linking of the cluster in the model cell with all of its images in the neighboring cells. The moment of the formation of such a cluster in 2D geometry is depicted in Fig. 3. However, the formation of an infinite connected structure at $N_p = N_1$ does not guarantee a sufficiently homogeneous distribution of the particles in the model cell. Figure 3 shows the presence of large pores, the size of which (at least in one direction) is comparable to the size of the model cell. Further addition of the particles leads to a rapid tightening of large pores, which (from "the point of view" of the algorithm used) are the pores with the sizes, that are substantially larger than the parameter r_{meso}. As a result, the algorithm makes it possible to create a porous structure with a characteristic pore size comparable to the value of the parameter r_{meso}. In other words, the adjustment of r_{meso} allows controlling the mesostructure of the systems being generated. However, the study of the systems with a pronounced mesostructure (i.e., with large pores) requires large model cells. The inequality of $L_{\text{cell}} \gg r_{\text{meso}}$ is advisable. The simulation of such a system is extremely time consuming. Therefore, in order to reduce a calculation time in this study the parameter r_{meso} has been set to a sufficiently smaller value ($r_{\text{meso}} = 2d$), when the mesostructure hardly manifests itself.

A sensitive parameter, reflecting the distribution of the particles in the model cell, is the radial distribution function

$$g(r) = \frac{v_0 dN}{\rho dV}, \quad \rho = 1 - \theta = \frac{v_0 N_p}{V_{\text{cell}}}, \tag{13}$$

where $v_0 = (\pi/6)d^3$ is the volume of a particle; dN is a number of the particles, which fall into a spherical layer $dV = 4\pi r^2 dr$ with the center at the given particle; ρ is the density, i.e., the volume fraction occupied by the particles, θ is the porosity, i.e., the volume fraction of the pores, and V_{cell} is the volume of the model cell. Averaging functions $g(r)$ over all particles of the system, we obtain a more convenient expression for calculations:

$$g(r) = \frac{v_0 dM}{\rho N_p 4\pi r^2 dr}, \tag{14}$$

where dM is the double number of the pairs of the particles, the distance between which falls within the range $(r - dr/2, r + dr/2)$. The last equation allows gathering statistics much faster than Eq. (13). Figure 4 demonstrates the functions $g(r)$ calculated by Eq. (14) for 3D structures. In general, they exhibit well-known features of monosized systems [30,40,62]: the δ-function region at $r = r_{eq}$ and the split-second peak at $r/r_{eq} = \sqrt{3}$ and 2, which "is a clear signature of the strong local order in the first two coordination shells of the packing" [62].

The model cell can be considered as a representative element if its size is much larger than the correlation distance

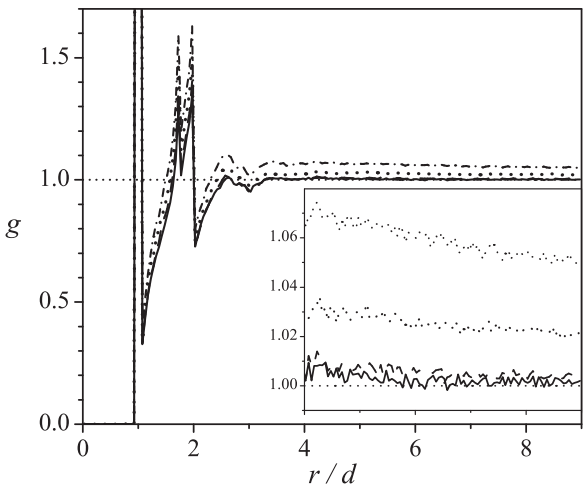

FIG. 4. Radial distribution functions in 3D geometry for different densities ρ_0 of initial structures: $\rho_0 = 0.24$ (solid lines), 0.22 (dashed lines), 0.20 (dotted lines), and 0.18 (dashed-dotted lines). The inset shows the region $4 \leqslant r/d \leqslant 9$ in an enlarged scale. Each line is constructed by averaging over ten independent numerical experiments. The simulation parameters are $N_p = 8000$, $r_{\text{meso}} = 2d$, and the horizontal sizes of the model cell are $x_{\text{cell}} = y_{\text{cell}} = 18d$.

of the particles and, in particular, the size of the structural elements of the modeled system, i.e., the size of the pores. These conditions are easily controlled by the form of the radial distribution function: at the distance of $L_{\text{cell}}/2$ (half of the minimum size of the cell) the function $g(r)$ should surely achieve its asymptotic value equal to unity. Figure 4 shows that in 3D geometry at densities $\rho < 0.22$ the radial functions do not achieve asymptotic value [$g(r) \not\to 1$ at $r = L_{\text{cell}}/2$], i.e., there are large pores in the model cell. Starting with the density $\rho = 0.24$ the function $g(L_{\text{cell}}/2) = 1$ within the statistical error, i.e., a sufficiently homogeneous particle distribution is achieved. According to this the value of $\rho_0 = 0.24$ was set as the initial density of the powder systems simulated for further analysis. It can be noted that the oscillations of the radial distribution function $g(r)$ of the initial structures (with the parameter $r_{\text{meso}} = 2d$) almost disappear at the distance $r = 6d$. Therefore, for the analysis of the low-density states (with $\rho \simeq 0.2$–0.5) it would be enough to take model cells with the size of $L_{\text{cell}} = 12d$. However, the increase of the density (as will be demonstrated below) leads to the increase of the oscillatory behavior of the function $g(r)$ and to the increase of the correlation distance. That is why we use larger cells with the minimal size of $L_{\text{cell}} = 18d$.

IV. CALCULATION PROCEDURE

The periodic boundary conditions are imposed at the sides of a model cell. A compression step of a model cell is implemented by a simultaneous reduction of the cell size (all sizes when simulating the isotropic compaction; the cell height z_{cell} when simulating the uniaxial compaction; and so on) by 0.1% of the current value and the proportional resizing of the coordinates of all particles. New equilibrium positions of all particles are determined after each compression step. This procedure corresponds to the powder compaction in quasistatic conditions [3,4,6,16,17]. As known [30], the algorithm without inertia is convenient to simulate such a process, i.e., the displacements Δr_i of the particles are set proportionate to the forces acting,

$$\Delta \mathbf{r}_i = k\mathbf{f}_i, \quad \mathbf{f}_i = \sum_j \mathbf{f}_{ij}. \tag{15}$$

The maximum force f_i is determined to specify a concrete value of the proportionality coefficient k, which is the same for all particles. The value of k is set in such a way that the displacement of the ith particle under the maximum force f_i is equal to $(d - r_{eq})/2$. The rate of the force change is also taken into account, namely, the ith particle is not moved farther than the position, where the minimum of the absolute value of the force f_i is reached. As shown by the test runs, this procedure allows surely finding a new equilibrium position of the system at each compression step.

The stress tensor σ_{ij}, averaged over the model cell, is of great interest for the comparison with the experimental data. We calculate the stress tensor by the known expression [30–34]

$$\sigma_{ij} = \frac{-1}{V_{\text{cell}}} \sum_{k<l} f_i^{(kl)} r_j^{(kl)}, \tag{16}$$

where the summation is conducted over all pairs (k and l) of interacting particles.

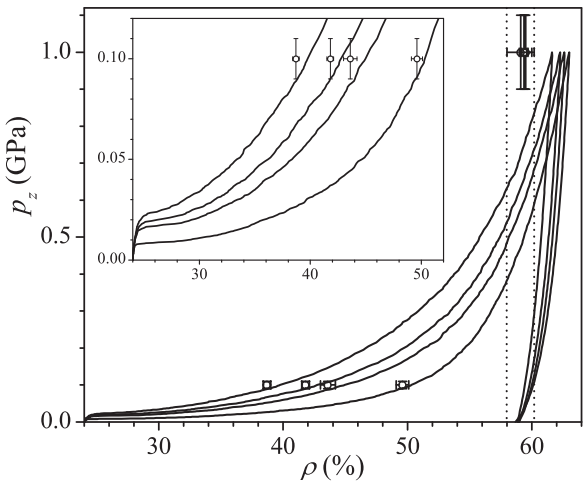

FIG. 5. The axial pressure $p_z = -\sigma_{zz}$ vs the powder density during uniaxial compaction along the Oz axis. The symbols are the experimental data of [25] on the compaction of alumina based nanopowders with a characteristic size of the particles $d = 9.7$, 16, 21, or 38 nm. The lines are the results of simulations of corresponding monosized model systems. The simulation parameters are $x_{\text{cell}} = y_{\text{cell}} = 18d$; $N_p = 8000$; $r_{\text{meso}} = 2d$; $\rho_0 = 0.24$; $\mu = 0.1$; $\Delta r_{ch} = 0.008d$; $\sigma_b = 0.018E$. The inset shows the small pressure region in an enlarged scale.

V. UNIAXIAL POWDER COMPACTION

We have performed a simulation of the uniaxial compaction of alumina based powders with a particle size of $d = 9.7$, 16, 21, or 38 (nm), for which we have experimental data (see Ref. [25]), to verify the theoretical model presented in the previous sections. The simulations have been performed both with and without the formation of solid bridges between the particles. In the latter case the parameter Δr_{ch} is set by unattainable large value (equal to the diameter of the particles). Figures 5 and 6 demonstrate the simulation results compared to the experimental data [25].

Figure 5 shows the compaction curves of the systems simulated in the coordinates of the "density vs uniaxial pressure ($p_z = -\sigma_{zz}$)." In order to reduce the errors of the calculation, each of the curves in the figure is constructed by averaging of the calculation data on the compaction of ten macroscopically equivalent but statistically independent model cells. The experimental data of Ref. [25] at pressure $p_z = 100$ MPa demonstrate clearly the size effect in the nanopowder compaction processes: the smaller the particle size the lower the density achieved. For example, the density of the powder with the particle size of $d = 9.7$ nm under the compression by the pressure of $p_z = 100$ MPa is 38.7%, while for the powder with 38-nm particles the density is 49.6%, i.e., the difference of the densities is $\Delta\rho = 10.9\%$. When increasing the compaction pressure up to $p_z = 1$ GPa the size effect vanishes, i.e., the densities of all powder compacts are identical within the experimental error.

In the theoretical model, when the formation and destruction of solid bridges is taken into account, the values of μ, Δr_{ch}, and σ_b play the role of free parameters (up to some limits). Figures 5 and 6 show that the theoretical model makes it possible to reproduce the experimental data [25] to high

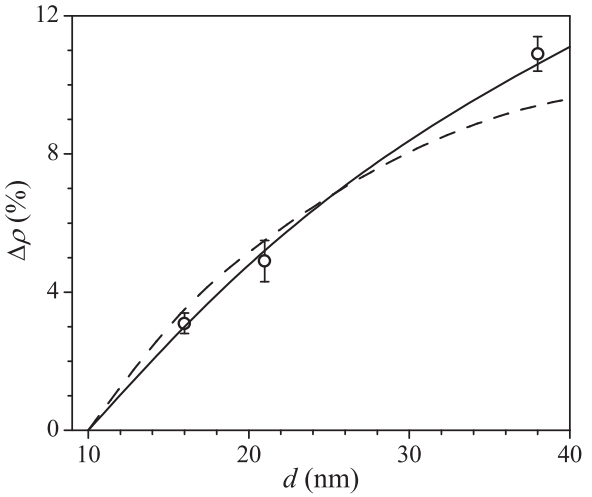

FIG. 6. The density difference $\Delta\rho = \rho(d) - \rho(d_1)$ after the uniaxial compaction up to the pressure $p_z = 100$ MPa between the powder systems with the particle size of d and $d_1 = 9.7$ nm. The symbols are the experimental data of [25]. The solid line is the simulation result (simulation parameters are the same as in Fig. 5). The dashed line is the result of simulations by the granular dynamics method without the formation of the solid bridges between the particles (the modified parameters are $\mu = 0.4$; $\Delta r_{ch} = 1.0d$).

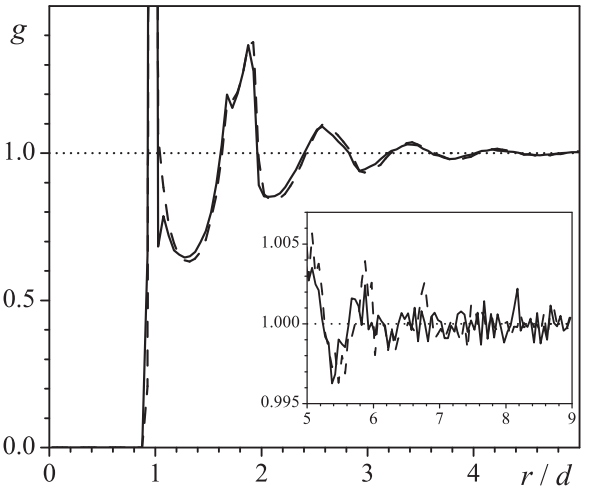

FIG. 7. The radial distribution functions at pressure $p_z = 1.0$ GPa for the model systems with a particle size of $d = 9.7$ nm (solid curve) and 38 nm (dashed curve). The simulation parameters are the same as in Fig. 5. The inset shows the region $5 \leqslant r/d \leqslant 9$ in an enlarged scale.

precision. This is achieved at the values of free parameters, $\mu = 0.1$, $\Delta r_{ch} = 0.008d$, and $\sigma_b = 0.018E$, which appear to be quite reasonable. It is worth noting that at pressure of $p_z = 1.0$ GPa the density differences between the model systems remain, for example, it is equal to 1.5% between the systems with $d = 38$ nm and $d = 9.7$ nm. But after the unloading of the model systems (removal of the axial pressure) the density differences disappear completely. It should be noted also that unloading from the level of $p_z = 100$ MPa (these lines are not shown in Fig. 5) leads to a reduction of the densities of all model systems by about 0.6%.

When the formation of solid bridges is not taken into account, i.e., at $\Delta r_{ch} = 1.0d$, there is only one free parameter in the theoretical model. It is the friction coefficient μ. The best agreement with the experimental data is reached at $\mu = 0.4$. In this case the compaction curves $p_z(\rho)$ are rather close to the corresponding curves shown in Fig. 5. This indicates that for a qualitative description of the size effect in the compaction processes of oxide nanopowders it is sufficient to consider the presence of the dispersion forces of attraction only. If a quantitative description is required, the disregard of the bridge formation reduces the model flexibility, as Fig. 6 illustrates. Here the density differences between the powder systems with different particle size at the compaction pressure $p_z = 100$ MPa are presented. Within the model without bridge formation, for example, the density difference between the systems with a particle size of 38 and 9.7 nm is equal to 9.4%, which is noticeably lower than the data of natural experiments (10.9%).

Figures 7 and 8 demonstrate such structural characteristics of the powder systems studied as the radial distribution function and the average coordination number. Figure 7 shows that the particle size and, therefore, the amplitude of the dispersion forces of attraction have a little effect on the form of the radial distribution function. As the powder is condensed the partial short-range ordering begins to appear. In comparison with the initial structure (see Fig. 4) the dependencies of $g(r)$ at the pressure of $p_z = 1.0$ GPa disclose the fourth and fifth peaks in addition to the first three. Nevertheless, the oscillations of the function $g(r)$ fade quickly and at the distances $r > 8d$ within the statistical error we have $g(r) = 1$. In particular, this fact means that the model cell with minimal size equal to $18d$ is certainly a representative element of a powder system. Figure 8 shows that the average coordination number k is more sensitive to the particle size than the radial distribution function. Although all model systems have almost the same value $k = 4$ from the beginning, a noticeable difference between them appears upon compaction. For example, when the pressure reaches $p_z = 1.0$ GPa we have $k = 6.56$ for the system with

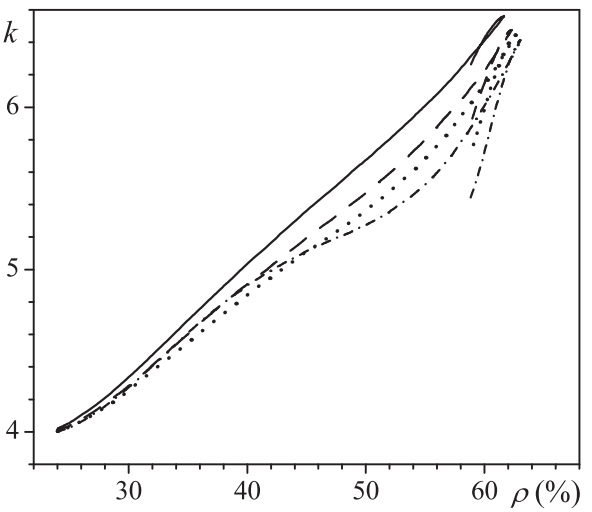

FIG. 8. The average coordination number vs the density of the model systems with $d = 9.7$ nm (solid line), 16 (dashed line), 21 (dotted line), and 38 (dashed-dotted line). The simulation parameters are the same as in Fig. 5.

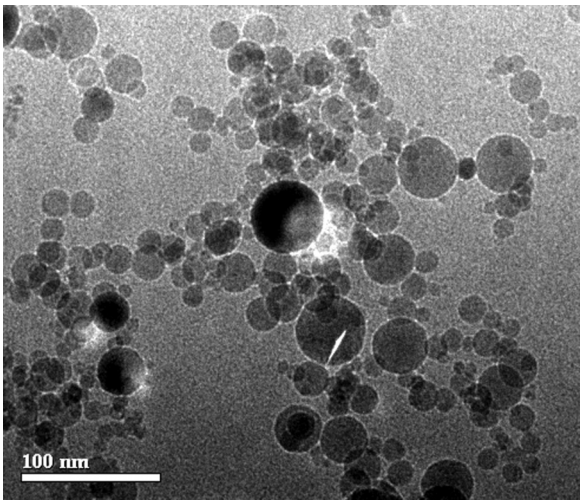

FIG. 9. SEM micrograph of Al_2O_3 powder.

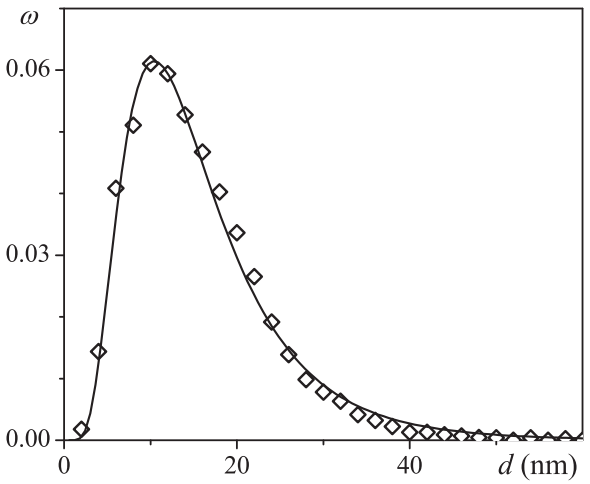

FIG. 10. The size distribution of Al_2O_3 powder particles obtained by laser target evaporation. The symbols are the results of micrographs processing; the line is the approximation by the log-normal distribution function (17) with parameters $\sigma = 0.547$ and $m = 2.644$.

a particle size $d = 9.7$ nm and $k = 6.41$ for the system with $d = 38$ nm. The difference increases yet more after unloading, where we have $k = 6.26$ and $k = 5.41$ for those systems. As a whole, the relatively low values of the average coordination number are an indication of quite irregular structures, where the regions of close-packed particles are absent. For example, at the compaction pressure of $p_z = 1.0$ GPa the share of the particles with the coordination number of 10 is only 0.5% for the system with $d = 9.7$ nm and 0.3% for the system with $d = 38$ nm. The particles having 12 contacts are absent.

VI. COMPARISON OF UNIAXIAL, BIAXIAL, AND ISOTROPIC COMPACTION PROCESSES

The natural and numerical experiments have been performed on the effect of the conditions of the compaction process, i.e., on the comparison of such processes as the uniaxial compaction, the biaxial (radial) compaction, or the isotropic (isostatic) compaction to further verify the theoretical model. In the course of natural experiments the closed-die compaction and cold isostatic pressing of Al_2O_3 nanopowders (phase composition is $0.9\gamma + 0.1\delta$) and 1% Nd:Y_2O_3 (yttrium oxide doped by 1% of neodymium in the monoclinic phase) have been performed. The powders were obtained in the Institute of Electrophysics (Ural Branch of RAS) by the target evaporation with a pulse-periodic CO_2 laser, followed by the subsequent condensation in the air stream [63,64]. The particle size analysis of the powders was performed with a scanning microscope. Figure 9 shows a typical image. As can be seen, the powders display weak agglomeration that is characteristic for the target evaporation method [63,64]. Computer processing of the images allowed constructing the size distribution of the powders, see Fig. 10, which was adequately fitted by a log-normal distribution,

$$\omega(x) = \frac{1}{x\sigma\sqrt{2\pi}} \exp\left[-\frac{(m - \ln x)^2}{2\sigma^2}\right]. \qquad (17)$$

In particular, the fitted parameters are $\sigma = 0.547$ and $m = 2.644$ for the Al_2O_3 powder. The characteristic size of the particles, where the maximum of the function $\omega(x)$ is located, is $d \simeq 10.4$ nm. The Y_2O_3 nanopowder is characterized by close values of the parameters.

During the natural experiments the powders were subjected to pressures of 100, 150, and 200 MPa. The closed-die compaction was performed in a hydraulic decimal press DP-36. Here the powder was placed into the cylindrical hole (14 mm in diameter) of a metal mold, and the external pressure p_z was applied to the upper movable punch. The isostatic pressing ($p_x = p_y = p_z$) was performed by an original izostate based on the hydraulic machine NGR-2000. Here the powder was packed in an impermeable flexible latex envelope. The ethylene glycol was the working fluid of the hydrostat. Figure 11 presents the experimental results in the "density vs pressure p_z" coordinates.

As compared to the powders obtained by the wire explosion method, those compaction experimental data [25] have been shown in Fig. 5, the nanopowder used in the present study has a much higher density in the pressure range investigated. Thus, according to Ref. [25] at pressure $p_z = 100$ MPa the density of the powder with the particle size $d = 10$ nm amounts to 38.7%, while now we have $\rho \simeq 50.5\%$ for the powder with $d = 9.7$ nm under uniaxial compaction. The difference in compressibility of the powders obtained by different methods can appear due to the influence of gases adsorbed on the surfaces of the powder particles. According to Ref. [63] the mass fraction of the adsorbates in Al_2O_3 nanopowders obtained by the target evaporation is about 5%. The cleaning of the particle surface, which is necessary, for example, in the production of laser ceramics [64], occurs usually during the powder annealing. However, in this study, the annealing has not been performed to keep a low powder agglomeration.

In terms of the theoretical model the high content of the adsorbates on the particle surface makes the formation of solid bridges difficult (that is why there is no agglomeration of the powder; see Fig. 9) and has an influence on the effective values of the friction coefficient (μ) and the parameter α. The latter determines the minimum distance between the powder particles, $h_0 = \alpha d_0$, which is considered as the contact of

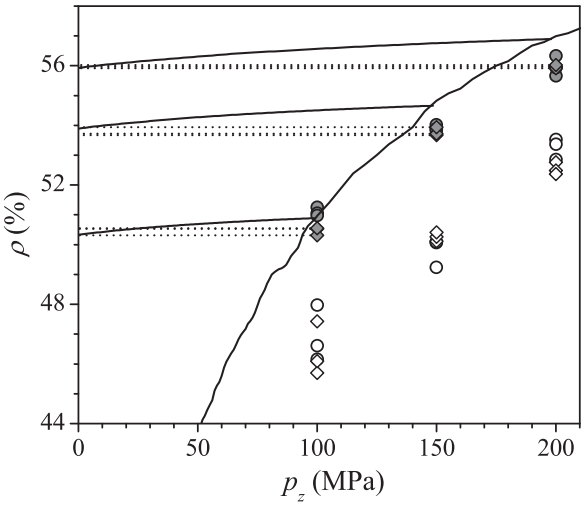

FIG. 11. The powder density ρ vs the external pressure p_z. The symbols are the experimental data on the uniaxial compaction (diamonds) and the isotropic compaction (circles) for the Al_2O_3 powders (grey dots) and Y_2O_3 powders (open dots). The lines are the results of computer simulations of uniaxial compaction of Al_2O_3 powder: the curve of monotonic loading and the curves of elastic unloading from the levels of $p_z = 100$, 150, and 200 MPa are shown. The simulation parameters are $\Delta r_{ch} = 1.0d$ (i.e., there are no solid bridges between particles); $\varepsilon = 1224k_B$, $d = 10.4$ nm, $\mu = 0.13$, $\alpha = 0.37$.

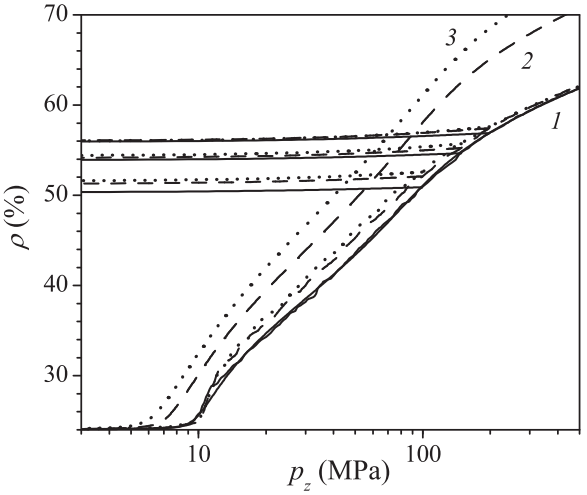

FIG. 12. The comparison of the uniaxial (solid lines), biaxial (dashed lines), and isotropic (dotted lines) compaction processes in the density vs pressure p_z coordinates. The numbered lines have been calculated within the continuum theory of plastically hardened porous body, Eqs. (20)–(23). The unnumbered lines are simulations by the granular dynamics method (here, in addition to the loading curves, the curves of elastic unloading from the levels of $p_z = 100$, 150, and 200 MPa have been shown). The simulation parameters are the same as in Fig. 11.

particles. The value $\alpha = 0.24$ was obtained in Refs. [23,24,53] with the reference to the clean surfaces of the particles, when nothing prevented its connection. The presence of adsorbates should increase the minimum distance between the particles, i.e., the value of α. Hence, in order to describe the experimental data on uniaxial compaction of Al_2O_3 nanopowder the value of Δr_{ch} was equate with the particles's diameter, which excludes the possibility of the bridge formation, and the quantities μ and α were playing the role of free parameters.

The best description of the experimental data has been obtained with the following values: $\mu = 0.13$ and $\alpha = 0.37$. Figure 11 shows the results of computer simulations at these parameters in comparison with the experimental data. The theoretical curves in the figure have been constructed by the averaging over ten independent simulations. In addition to the monotonic loading curve, the lines of elastic unloading have been presented, where the external axial pressure p_z is decreased from the values of 100, 150, and 200 MPa down to zero. It is the powder density, realized by the pressure release (the unloading density), which should be compared to the experimental data, since the latter are also obtained from the analysis of the unloaded compacts. Figure 11 shows that the theoretical model can reproduce the experimental data with high accuracy, the error in the density is less than the scattering of the experimental points.

The theoretical model with the fixed parameters μ and α has been used to study the powders compaction in other geometries of the external load (not uniaxial): the biaxial (or radial) load, when the model cell is compressed along two axes (Oz and Oy), and the isotropic (or isostatic) load. Figure 12 demonstrates the simulation results. A joint analysis of the experimental data, presented in Fig. 11, and the simulation curves in Fig. 12 show a complete consent of them. It turned out that the density of oxide nanopowders (Al_2O_3 or Y_2O_3) depends very weakly on the geometry of the external load. Both the simulation and the natural experiments reveal a little difference (less than 1%) between the unloading densities of the compacts after isostatic or uniaxial compaction with the pressure of $p_z = 100$ MPa. When the maximal pressure p_z is raised up to 200 MPa, these differences disappear completely.

It should be noted that the observed insensitivity of oxide nanopowders to the geometry of external loads is very surprising. In order to describe the mechanical properties of the powder bodies a continuum theory of plastically hardening porous body [5,9,10] is usually applied. This theory describes the compaction processes of micron sized and coarser powders. According to the continuum theory, the border between the regions of the elastic and plastic deformation of the body, i.e., the loading surface, is given by

$$\frac{p^2}{\Psi} + \frac{\tau^2}{\phi} = (1-\theta)\tau_0(\gamma_0), \tag{18}$$

where $p = -\mathrm{Sp}\,(\sigma_{ij})/3$ is the hydrostatic part of the stress tensor, $\tau = \sqrt{\tau_{ij}\tau_{ji}}$ is the intensity of the stress deviator ($\tau_{ij} = \sigma_{ij} + p\delta_{ij}$, δ_{ij} is the unit tensor), τ_0 is the yield strength of the solid phase of the porous body. The measure of the accumulated shear deformation of the solid phase, γ_0, is given by the relations

$$\gamma_0 = \int_0^t \dot{\gamma}_0 dt, \quad (1-\theta)\dot{\gamma}_0^2 = \Psi\dot{e}^2 + \phi\dot{\gamma}^2, \tag{19}$$

where $\dot{e} = \mathrm{Sp}\,(\dot{e}_{ij})$ and $\dot{\gamma}$ are the first invariant of the strain rate tensor and the intensity of its deviator, respectively. The functions of porosity, $\Psi(\theta)$ and $\phi(\theta)$, which are in Eqs. (18) and (19), have been established in Ref. [11] within the

hydrodynamic analogy with the theory of elasticity, and can be presented in the form of [6]

$$\phi = (1-\theta)^{5/3}, \quad \Psi = \frac{2}{3}\frac{1-\theta+\theta^2/2}{\theta}\,\phi. \tag{20}$$

Eqs. (18)–(20), together with the associated flow law, give

$$\begin{aligned} p_z &= \sqrt{\Psi + \frac{2}{3}\phi}\,\sqrt{1-\theta}\,\tau_0(\gamma_0), \\ \gamma_0 &= \int_\theta^{\theta_0} \sqrt{\Psi + \frac{2}{3}\phi}\,\frac{d\theta}{(1-\theta)^{3/2}}, \end{aligned} \tag{21}$$

for the process of uniaxial compression along the axis of Oz;

$$\begin{aligned} p_z = p_y &= \sqrt{\Psi + \frac{1}{6}\phi}\,\sqrt{1-\theta}\,\tau_0(\gamma_0), \\ \gamma_0 &= \int_\theta^{\theta_0} \sqrt{\Psi + \frac{1}{6}\phi}\,\frac{d\theta}{(1-\theta)^{3/2}}, \end{aligned} \tag{22}$$

for the process of biaxial compression along Oz and Oy axes; and

$$\begin{aligned} p_z = p_y = p_x &= \sqrt{\Psi}\,\sqrt{1-\theta}\,\tau_0(\gamma_0), \\ \gamma_0 &= \int_\theta^{\theta_0} \sqrt{\Psi}\,\frac{d\theta}{(1-\theta)^{3/2}}, \end{aligned} \tag{23}$$

in the case of the isostatic compression.

The dependence of $\tau_0(\gamma_0)$, the so-called hardening law of the material, is not determined within the continuum theory, i.e., it is an input parameter of the theory. As a rule, the hardening law is established empirically. We can determine the dependence of $\tau_0(\gamma_0)$ from any of the simulation curves obtained by the granular dynamics method, for example, from the curve of uniaxial compaction. After that the continuum theory in accordance with Eqs. (20)–(23) determines uniquely the powder behavior at other loading geometries. Figure 12 shows the curves calculated in this way (the numbered lines). As can be seen, the traditional continuum theory predicts an appreciable influence of the loading geometry on the final porosity of the compacts. For example, in the pressure range investigated (p_z = 100–200 MPa), it predicts the difference in density between the isostatic and the uniaxial compaction processes of about 10%, i.e., the transition from the geometry of the uniaxial compaction to the biaxial process, and then to the isostatic process, should significantly increase the density of the compacts. This theoretical prognosis conforms to the behavior of the coarse powders, where the difference in the density between the uniaxial and the isostatic compaction processes is just about 10% [65].

Contrary to the predictions of the continuum theory, the oxide nanopowders studied, as Fig. 11 shows, have a qualitatively different behavior, namely, they display the extremely low sensitivity to the geometry of the external loads. On one hand, it is the evidence of the inapplicability of the traditional continuum theories to describe the mechanical properties of these powders. On the other hand, it emphasizes the high reliability of the simulations within the theoretical model developed, which makes it possible to reproduce this specific behavior of oxide nanopowders to high precision.

The insensitivity of the powder density with respect to the geometry of loading seems to bring the powder behavior to the fluid one, for which, in particular, the stress tensor in the static limit is always spherical irrespective of the scheme of the external loads. However, Figs. 13 and 14 prove that for the nanopowders this is not the case. Figure 13 shows that in the powders studied there is no evening the stresses in different directions. The lateral pressure $p_x = -\sigma_{xx}$ (in the direction of the Ox axis, where there is no compression of the model cells) under the uniaxial or biaxial compaction is significantly lower than the axial pressure $p_z = -\sigma_{zz}$. At the microlevel, this is expressed in the emergence of an appreciable anisotropy induced by the compaction processes. As the anisotropy illustration, Fig. 14 shows a strong angular dependencies of the contact forces in the system after the uniaxial and biaxial compaction processes.

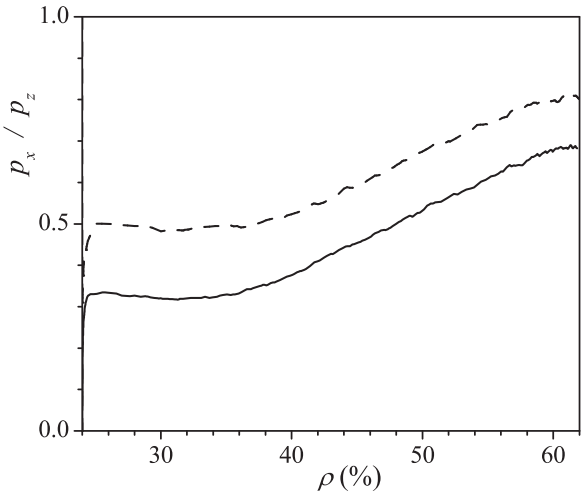

FIG. 13. The ratio of the lateral ($p_x = -\sigma_{xx}$) to the axial (p_z) pressures vs the density. The solid line is for the uniaxial compression of the model cell along the Oz axis; the dashed line is for the biaxial compression along the Oz and Oy axes. The simulation parameters are the same as in Fig. 11.

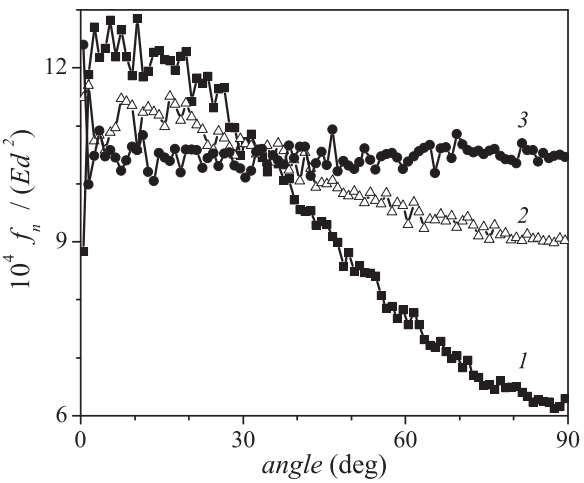

FIG. 14. The average force of the particles normal interactions $f_n = f_e - f_a$ vs the angle between the contact axis and the vertical axis Oz at the external pressure p_z = 500 MPa for uniaxial /1/, biaxial /2/, and isotropic /3/ compactions. The simulation parameters are the same as in Fig. 11.

VII. CONCLUSION

A discrete theoretical model of a powder body has been presented. The model makes it possible to reproduce the mechanical properties of the oxide nanopowders to high precision. The verification of the model has been performed by the experimental data on the compaction of alumina based nanopowders and 1% Nd:Y_2O_3 nanopowders (yttrium oxide doped by 1% of neodymium). It is shown that the model describes reliably such specific features of nanopowder behavior as the size effect and the low sensitivity to the geometry of loading (uniaxial, biaxial, or isotropic compression).

The main results of the research are as follows:

(1) The origin of the size effect in the processes of the cold compaction of dry oxide nanopowders is the dispersion forces of interparticle attractions (van der Waals–Hamaker interactions). It is sufficient to take into account these interactions in the theoretical model in order to describe the size effect on a qualitative level. However, the accurate (quantitative) analysis of easily aggregating nanopowders (for example, annealed powders with an adsorbates-free surface) requires the introduction to a theoretical model of the possibility of formation and destruction of stronger interparticle bonds of chemical nature.

(2) The oxide nanopowders exhibit very low sensitivity to the geometry of compression: the differences in the density of the compacts at a fixed level of external load for the schemes of uniaxial and isostatic compaction are less than 1%. Such behavior is qualitatively different from the one of micron sized or coarser powders and is not described by the continuum theory of plasticity of hardening porous body, which is traditionally used to describe the mechanical properties of the powder bodies.

ACKNOWLEDGMENTS

The authors thank V. V. Platonov and O. R. Timoshenkova for the particle size analysis of the nanopowders studied. The work was supported by the RFBR (Projects No. 12-08-00298 and No. 11-08-00005) and the Presidium of the Ural Branch of RAS (Project No. 12-C-2-1018).

[1] R. W. Siegel, Nanostruct. Mater. **4**, 121 (1994).
[2] R. A. Andrievskii and A. V. Ragulya, *Nanostructured Materials* (Akademiya, Moscow, 2005) (in Russian).
[3] V. V. Ivanov, V. R. Khrustov, S. N. Paranin, A. I. Medvedev, A. K. Shtol'ts, O. F. Ivanova, and A. A. Nozdrin, Glass Phys. Chem. **31**, 465 (2005).
[4] V. R. Khrustov, V. V. Ivanov, Y. A. Kotov, A. S. Kaigorodov, and O. F. Ivanova, Glass Phys. Chem. **33**, 379 (2007).
[5] M. B. Shtern, G. G. Serdyuk, L. A. Maksimenko, Y. V. Truhan, and Y. M. Shulyakov, *Phenomenological Theories of Powder Pressing* (Naukova Dumka, Kiev, 1982) (in Russian).
[6] G. S. Boltachev, N. B. Volkov, S. V. Dobrov, V. V. Ivanov, A. A. Nozdrin, and S. N. Paranin, Tech. Phys. **52**, 1306 (2007).
[7] G. S. Boltachev, N. B. Volkov, V. V. Ivanov, and S. N. Paranin, J. Appl. Mech. Tech. Phys. **49**, 336 (2008).
[8] G. S. Boltachev, N. B. Volkov, V. V. Ivanov, and S. N. Paranin, J. Adv. Mater. **5**, 5 (2008) (in Russian).
[9] E. A. Olevsky, G. Timmermans, M. B. Shtern, L. Froyen, and L. Delaey, Powder Technol. **93**, 127 (1997).
[10] A. L. Maximenko, E. A. Olevsky, and M. B. Shtern, Comput. Mater. Sci. **43**, 704 (2008).
[11] V. V. Skorokhod, *Rheological Principles of Sintering Theory* (Naukova Dumka, Kiev, 1972) (in Russian).
[12] E. A. Olevsky and M. B. Shtern, Powder Metall. Metal Ceram. **43**, 355 (2004).
[13] M. B. Shtern, Powder Metall. Metal Ceram. **31**, 735 (1992).
[14] V. P. Filonenko, L. G. Khvostantsev, R. K. Bagramov, L. I. Trusov, and V. I. Novikov, Powder Metall. Metal Ceram. **31**, 296 (1992).
[15] V. G. Gryaznov, A. M. Kaprelov, and A. E. Romanov, Pis'ma Zh. Tekh. Fiz. **15**, 39 (1989).
[16] R. Vassen and D. Stoever, Powder Technol. **72**, 223 (1992).
[17] M. Zhao, X. Li, Z. Wang, L. Song, L. Xiao, and B. Xu, Nanostruct. Mater. **1**, 379 (1992).
[18] M. I. Alymov, V. A. Zelenskii, and E. I. Maltina, Phys. Chem. Mater. Process. **3**, 154 (1993) (in Russian).
[19] M. I. Alymov, *Powder Metallurgy of Nanocrystal Materials* (Nauka, Moscow, 2007) (in Russian).
[20] A. Balakrishnan, P. Pizette, C. L. Martin, S. V. Joshi, and B. P. Saha, Acta Mater. **58**, 802 (2010).
[21] K. Z. Y. Yen and T. K. Chaki, J. Appl. Phys. **71**, 3164 (1992).
[22] A. B. Yu, C. L. Feng, R. P. Zou, and R. Y. Yang, Powder Technol. **130**, 70 (2003).
[23] G. S. Boltachev and N. B. Volkov, Tech. Phys. Lett. **36**, 823 (2010).
[24] G. S. Boltachev and N. B. Volkov, Tech. Phys. **56**, 919 (2011).
[25] G. S. Boltachev, N. B. Volkov, A. S. Kaygorodov, and V. P. Loznukho, Nanotechnol. Russ. **6**, 639 (2011).
[26] G. S. Boltachev and N. B. Volkov, Powder Metall. Metal Ceram. **51**, 260 (2012).
[27] P. A. Cundall and O. D. L. Strack, Geotechnique **29**, 47 (1979).
[28] J. Lian and S. Shima, Int. J. Numer. Methods Eng. **37**, 763 (1994).
[29] R. Y. Yang, R. P. Zou, and A. B. Yu, Phys. Rev. E **62**, 3900 (2000).
[30] I. Agnolin and J.-N. Roux, Phys. Rev. E **76**, 061302 (2007).
[31] I. Agnolin and J.-N. Roux, Phys. Rev. E **76**, 061303 (2007).
[32] I. Agnolin and J.-N. Roux, Phys. Rev. E **76**, 061304 (2007).
[33] F. A. Gilabert, J.-N. Roux, and A. Castellanos, Phys. Rev. E **75**, 011303 (2007).
[34] F. A. Gilabert, J.-N. Roux, and A. Castellanos, Phys. Rev. E **78**, 031305 (2008).
[35] S. Luding, Gran. Matter **10**, 235 (2008).
[36] S. J. Antony and N. P. Kruyt, Phys. Rev. E **79**, 031308 (2009).
[37] E. Medina, X. Garcia, and V. Urdaneta, Phys. Rev. E **81**, 022301 (2010).
[38] J. Baxter, U. Tuzun, J. Burnell, and D. M. Heyes, Phys. Rev. E **55**, 3546 (1997).

[39] T. S. T. Poschel, *Computational Granular Dynamics. Models and Algorithms* (Springer, Berlin, 2005).
[40] L. F. Liu, Z. P. Zhang, and A. B. Yu, Physica A: Stat. Theor. Phys. **268**, 433 (1999).
[41] H. Hertz, J. Reine Angew. Math. **92**, 156 (1881).
[42] C. Cattaneo, Accad. Lincei, Rend. Ser. 6 **27**, 342, 434, and 474 (1938).
[43] R. D. Mindlin, J. Appl. Mech. (Trans ASME) **16**, 259 (1949).
[44] R. D. Mindlin and H. Deresiewicz, J. Appl. Mech. (Trans ASME) **20**, 327 (1953).
[45] G. S. Boltachev, K. E. Lukyashin, A. S. Shirinyan, V. A. Shitov, and N. B. Volkov, in *Proceedings of IIIth International Conference Modern Problems of Condensed Matter* (Taras Shevchenko Kyiv National University, Kiev, 2012), p. 59.
[46] G. S. Boltachev, N. B. Volkov, K. E. Lukyashin, and V. A. Shitov, in *Proceedings of IIIth International Conference Nanostructured Materials—2012: Russia-Ukraine-Belarus (NANO-2012)* (LEMA, St. Petersburg, 2012), p. 38.
[47] R. M. McMeeking, G. Jefferson, and G. K. Haritos, in *Recent Developments in Computer Modeling of Powder Metallurgy Processes*, edited by A. Zavaliangos and A. Laptev (IOS, Amsterdam, 2001), pp. 50–62.
[48] G. Jefferson, G. K. Haritos, and R. M. McMeeking, J. Mech. Phys. Solids **50**, 2539 (2002).
[49] E. Dintwa, E. Tijskens, and H. Ramon, Gran. Matter **10**, 209 (2008).
[50] G. S. Boltachev, N. B. Volkov, E. G. Kirkova, M. B. Shtern, and A. V. Kuzmov, in *Proceedings of the EURO PM2011 Congress and Exhibition* (European Powder Metallurgy Association, Barcelona, 2011), pp. 43–48.
[51] G. S. Boltachev, N. B. Volkov, and N. M. Zubarev, Int. J. Solids Struct. **49**, 2107 (2012).
[52] H. C. Hamaker, Physica **4**, 1058 (1937).
[53] G. S. Boltachev, N. B. Volkov, and K. A. Nagayev, J. Colloid Interface Sci. **355**, 417 (2011).
[54] F. A. Gilabert, A. M. Krivtsov, and A. Castellanos, Meccanica **41**, 341 (2006).
[55] B. V. Derjaguin, V. M. Muller, and Y. P. Toporov, J. Colloid Interface Sci. **53**, 314 (1975).
[56] T. Namazu, Y. Isono, and T. Tanaka, J. Microelectromech. Syst. **9**, 450 (2000).
[57] S. A. Kotrechko, A. V. Filatov, and A. V. Ovsjannikov, Theor. Appl. Fract. Mech. **45**, 92 (2006).
[58] A. P. Shpak, S. O. Kotrechko, T. I. Mazilova, and I. M. Mikhailovskij, Sci. Technol. Adv. Mater. **10**, 045004 (2009).
[59] E. Reissner and H. F. Sagoci, J. Appl. Phys. **15**, 652 (1944).
[60] J. Jager, Arch. Appl. Mech. **65**, 478 (1995).
[61] A. I. Lur'e, *Three-Dimensional Problems of the Theory of Elasticity* (Interscience, New York, 1964).
[62] A. Donev, S. Torquato, and F. H. Stillinger, Phys. Rev. E **71**, 011105 (2005).
[63] Y. A. Kotov, V. V. Osipov, M. G. Ivanov, O. M. Samatov, V. V. Platonov, E. I. Azarkevich, A. M. Murzakaev, and A. I. Medvedev, Tech. Phys. **47**, 1420 (2002).
[64] A. S. Kaigorodov, V. V. Ivanov, V. R. Khrustov, Y. A. Kotov, A. I. Medvedev, V. V. Osipov, M. G. Ivanov, A. N. Orlov, and A. M. Murzakaev, J. Eur. Ceram. Soc. **27**, 1165 (2007).
[65] S. S. Kiparisov and G. A. Libenson, *Powder Metallurgy* (Metallurgia, Moscow, 1980) (in Russian).